

On velocity and migration structural uncertainties: A new approach using non-linear slope tomography

J  r  mie Messud, Patrice Guillaume, Gilles Lambar  
CGG, Massy

January 12, 2022

Evaluating structural uncertainties associated with seismic imaging and target horizons can be of critical importance for decision-making related to oil and gas exploration and production. An important breakthrough for industrial applications has been made with the development of industrial approaches to velocity model building. We propose here an extension of these approaches, using non-linear slope tomography (rather than standard tomographic migration velocity analysis as in previous publications). In addition to the advantages in terms of accuracy and efficiency of the velocity model building (compared to standard tomography) it can be used to assess the quality of standard uncertainty-related assumptions (linearity and Gaussian hypothesis within the Bayesian theory) and estimate volumetric migration positioning uncertainties (a generalization of horizon uncertainties). We derive and discuss the theoretical concepts underlying this approach and compare our derivations with those of previous publications. A main advantage is that we work directly in the full model space rather than in a preconditioned model space, (1) avoiding biased uncertainty analysis and (2) splitting the analysis into the resolved and unresolved tomography spaces. Another advantage is that, within the Bayesian formalism, we sample an equi-probable contour of the tomography posterior probability density function (pdf) rather than the full pdf, stabilizing the estimation of error bars. These advantages provide robustness to the approach. These concepts are illustrated on two different 3D field datasets. The first one illustrates structural uncertainties on a merge of different seismic surveys in the North Sea. The second one shows the impact of structural uncertainties on gross-rock volume computation.

Introduction

Decision-making and risk mitigation are critical for oil and gas exploration and production (E&P). Relying only on maximum-likelihood (or deterministic or single-valued) subsurface models can lead to drastic misinterpretations of the risk. Assessing uncertainties related to such maximum-likelihood models is therefore necessary [Simpson et al., 2000], but is a challenging task. Indeed, such single-valued models are built by long and complex processes where various types of information are combined sequentially. Seismic migration is a

central step within those processes, providing images of the general structure of the subsurface through a reflectivity model. The positioning uncertainties associated with the structures imaged in the reflectivity, or structural uncertainties, have been studied for decades [Hajnal and Sereda, 1981, Al Chalabi, 1994, Thore et al., 2002], in line with advances made in migration tools and workflows.

The key step affecting migration structural uncertainties is velocity model building (VMB). According to [Fournier et al., 2013] VMB is related to one of the biggest ambiguities impacting E&P. While we have seen over the last decade the development of full-wave VMB approaches [Virieux and Operto, 2009], ray-based reflection tomographic approaches remain an essential workhorse method [Woodward et al., 2008, Guillaume et al., 2013b, Lambaré et al., 2014]. This is due to their inherent characteristics, i.e. efficient numerical implementations, compressed kinematic data (picks) and ability to digest prior information. These advantages are particularly appealing from the perspective of a structural uncertainties analysis in an industrial context. An important contribution in terms of theory, implementation and application has been delivered by the work of [Osypov et al., 2008a, Osypov et al., 2008b, Osypov et al., 2010, Osypov et al., 2011, Osypov et al., 2013]. While there had been earlier investigations in the context of reflection tomography [Duffet and Sinoquet, 2006], to our knowledge [Osypov et al., 2008b] were the first to implement a tool used in the industry to estimate structural uncertainties associated with ray-based tomography. Their approach is based on the tomography toolbox described by [Woodward et al., 2008]. The uncertainty analysis is performed around the maximum-likelihood tomography model within a Bayesian approach, assuming a linearized modeling and a Gaussian probability density function (pdf). A partial eigen-decomposition of the tomography data operator is performed in a “model preconditioned basis” [Osypov et al., 2008b]. This allows the generation of perturbed tomography models related to a confidence level. Then map (or zero-offset kinematic) migrations of a target horizon within those models give a set of perturbed horizons. These are analyzed statistically to derive estimations of horizon error bars related to a confidence level. [Osypov et al., 2010, Osypov et al., 2011, Osypov et al., 2013] give details on practical aspects (such as calibrating the regularizations) and present applications relating to the assessment of oil reserves or well placement. This work demonstrated the affordability and effectiveness of the corresponding horizon uncertainty analysis for industrial applications.

To continue these efforts, our paper details some recent work on structural uncertainty analysis [Messud et al., 2017a, Messud et al., 2017b, Messud et al., 2018], with major differences compared to previous work. Firstly, while the work of [Osypov et al., 2008a, Osypov et al., 2010, Osypov et al., 2011, Osypov et al., 2013] was based on the classical (linear) tomographic approach described by [Woodward et al., 2008], our work is based on the non-linear slope tomography of [Guillaume et al., 2008, Lambaré et al., 2014]. An important advantage of non-linear tomography is the ability to compute all non-linear updates of the tomography model with only one picking step [Adler et al., 2008, Lambaré et al., 2014], whereas [Woodward et al., 2008] requires a new picking step (thus a new migration) for each iteration (or linear update). Also, non-linear slope tomography has the advantage of belonging to the family of slope tomography, where the model is recovered from picks of locally coherent reflected events in the pre-stack unmigrated domain [Lambaré, 2008]. In brief, the approach can extract in a non-linear way the kinematic information contained in a dense set of local picks. Numerous versions have been proposed covering a large set of configurations, i.e. multi-layer tomography [Guillaume et al., 2013a], dip-constrained tomography [Guillaume et al., 2013a], high-definition tomography [Guillaume et al., 2011] and joint direct and reflected wave tomography [Allemand et al., 2017].

In the context of structural uncertainty analysis, the non-linear approach provides an efficient way to QC the assumptions made within the Bayesian formalism (linearity and

Gaussian pdf hypothesis) [Messud et al., 2017a, Reinier et al., 2017]. It also makes it possible to derive volumetric migration positioning uncertainties, a volumetric generalization of the horizon positioning uncertainties that provides uncertainties also between horizons.

Secondly, our approach works directly in the full model space rather than in a pre-conditioned model space. This makes it possible to (1) avoid biased uncertainty analysis and (2) split the uncertainty analysis into resolved and unresolved tomography spaces. It also allows us, within the Bayesian formalism, to sample randomly a pdf’s equi-probable contour (related to a clear confidence level) rather than the full pdf [Osypov et al., 2013, Duffet and Sinoquet, 2002, Duffet and Sinoquet, 2006], providing more robust error bar estimates [Messud et al., 2017a, Messud et al., 2017b, Messud et al., 2018]. A general definition of error bars for a given confidence level is given (accounting for the non-diagonal part of the covariance matrices, avoiding underestimation). All this provides more generality and robustness to our approach than to previous efforts.

Our approach can easily apply to full-waveform inversion (FWI)-derived models. Indeed, these models usually go through a last tomography pass (FWI “post-processing”) in order to obtain flatter common image gathers. The corresponding tomography uncertainty analysis can then naturally be performed to produce an estimate for FWI model kinematic-related uncertainties. This workflow is practical as long as rays can adequately describe the kinematics of FWI-derived models.

Our paper carefully details the associated theoretical developments, providing a unifying framework to compare the approaches, in particular, the differences with [Osypov et al., 2008a, Osypov et al., 2010, Osypov et al., 2011, Osypov et al., 2013].

In the last part, we first present an application of the method to a North Sea 3D dataset: we show structural uncertainties in the image domain along selected horizons (positioned through zero-offset map migration) as well as volumetric migration positioning uncertainties associated with the tomography residual move-out (RMO) data (considering also non-zero offsets). We also illustrate the concepts of resolved and unresolved spaces uncertainties introduced in the theoretical sections. We then present an illustration on a second field 3D dataset of the impact of tomographic uncertainties on gross-rock volume (GRV) computation.

Tomography inverse problem

Non-linear slope tomography is a practical and efficient tool for velocity model building [Guillaume et al., 2013b]. Its input (or observed) data \mathbf{d}_{obs} consists of a set of picks or “kinematic invariants”, i.e. quantities that belong to the multi-dimensional unmigrated data domain. Invariants are described by source and receiver positions, two-way travel-times and time-slopes of locally coherent reflected events in the unmigrated domain. The invariants can be kinematically migrated in any (sufficiently smooth) model to deduce corresponding events or picks in the corresponding migrated domain ¹.

The tomography model \mathbf{m} consists of a set of parameters describing smooth velocity and anisotropy layers on a cardinal cubic bspline basis [Operto et al., 2003], separated by horizons. We denote by N_M the number of nodes that describe the model (in practice 500,000 to 50 million). The model is updated through a non-linear optimization scheme that aims to minimize among others the residual move-out, well misties, etc. The concept of invariants allows the implementation of an iterative non-linear inversion scheme where each linearized update consist of (1) a non-linear modeling (by finite-offset kinematic migration of the invariants) and a computation of tomography operator derivatives, and (2) a resolution

¹ The invariant can be measured either directly in the unmigrated time domain or indirectly in a prestack depth-migrated domain associated with a given model. In the latter case, measured quantities are kinematically de-migrated in the corresponding model to deduce the invariants.

of an inverse problem to deduce the update. After each linearized update, the data are modeled again non-linearly (by finite-offset kinematic migration) before a new inversion starts again. A simultaneous inversion of the model for all layers avoids the downward propagation of errors of a conventional top-down approach, and a multi-scale technique avoids getting trapped into a local minimum [Guillaume et al., 2013b]. The non-linear slope tomography is a flexible tool that drastically reduces the overall number of passes involving picking stages. It also makes it easier to fine-tune the regularizations and progressively reduce their level to let the data speak more.

The inversion scheme outputs to the maximum-likelihood tomography model \mathbf{m}^* , i.e. the model that fits the best the data under some prior constraints [Tarantola, 1986, Tarantola, 2005], that satisfies

$$\mathbf{m}^* = \arg \min_{\mathbf{m}} \frac{1}{2} \|\mathbf{C}_D^{-1/2}(\mathbf{d}_{obs} - \mathbf{d}(\mathbf{m}))\|_2^2 + \frac{1}{2} \|\mathbf{C}_M^{-1/2}(\mathbf{m} - \mathbf{m}_{prior})\|_2^2. \quad (1)$$

Here $\mathbf{d}(\mathbf{m})$ denotes the data modeled from a model \mathbf{m} . \mathbf{C}_D is the covariance matrix in the data space. It accounts for data (tomography picks) and modeling uncertainties. \mathbf{C}_M is the “prior” covariance matrix in the model space, associated with a prior model \mathbf{m}_{prior} . It helps regularization and accounts for uncertainties on the prior model. Non-zero non-diagonal elements of a covariance matrix \mathbf{C}_i mean that corresponding nodes are correlated. The diagonal elements of a covariance matrix \mathbf{C}_i are called variances, and the square roots of the variances are called standard deviations. In the following, bold lowercase letter quantities represent vectors and all bold uppercase letter quantities represent matrices.

Equation 1 is solved by a non-linear local optimization method, updating iteratively the model by

$$\mathbf{m}_{k+1} = \mathbf{m}_k + \delta \mathbf{m}_k, \quad (2)$$

where $k \in [0, n]$ denotes the iteration number and n the last iteration number. At the last tomography iteration, the obtained \mathbf{m}_n is considered to be the maximum-likelihood solution \mathbf{m}^* . In practice, the updates $\Delta \mathbf{m}_k$ in equation 2 are computed through a linearization of equation 1 at each iteration, solving

$$\min_{\delta \mathbf{m}_k} \|\mathbf{A}_k \delta \mathbf{m}_k - \mathbf{b}_k\|_2^2, \quad (3)$$

where \mathbf{A}_k is the Jacobian matrix and \mathbf{b}_k the “error vector”, containing information on the data and the prior (these terms are defined in the next paragraphs).

\mathbf{A}_k is defined by

$$\mathbf{A}_k = \begin{bmatrix} \mathbf{C}_D^{-1/2} \mathbf{G}_k \\ \mathbf{C}_R^{-1/2} \end{bmatrix}, \quad (4)$$

containing the tomography modeling Jacobian matrix at iteration k

$$\mathbf{G}_k = \left. \frac{\partial \mathbf{d}(\mathbf{m})}{\partial \mathbf{m}} \right|_{\mathbf{m}=\mathbf{m}_k}, \quad (5)$$

and $\mathbf{C}_R^{1/2}$ gathers various contributions to the prior covariance in model space or constraints

$$\mathbf{C}_R^{-1/2} = \begin{bmatrix} \mathbf{Damp} \\ \mathbf{Other}_1 \\ \vdots \\ \mathbf{Other}_{L-1} \end{bmatrix}$$

$$\mathbf{C}_M^{-1} = \mathbf{C}_R^{-1/2\dagger} \mathbf{C}_R^{-1/2} = \mathbf{Damp}^\dagger \mathbf{Damp} + \sum_{i=1}^{L-1} \mathbf{Other}_i^\dagger \mathbf{Other}_i, \quad (6)$$

where \dagger denotes transpose. Each of the L prior contributions (\mathbf{Damp} and \mathbf{Other}_i) is represented by a square matrix of size $N_M \times N_M$. \mathbf{Damp} represents a damping or diagonal matrix, scaled for each model contribution or subsurface parameter (velocity, various anisotropies, etc.). \mathbf{Other}_i represents other possible constraints, for instance, a Laplacian one and/or a structural one in our non-linear slope tomography. $\mathbf{C}_R^{-1/2}$ is a matrix of size $(L \times N_M) \times N_M$. Denoting by N_D the number of data, i.e. picks, \mathbf{A}_n is a matrix of size $(N_D + L \times N_M) \times N_M$.

The error vector has size $(N_D + L \times N_M)$ and is defined by

$$\mathbf{b}_k = \begin{bmatrix} \mathbf{C}_D^{-1/2}(\mathbf{d}_{obs} - \mathbf{d}(\mathbf{m}_k)) \\ \mathbf{C}_R^{-1/2}(\mathbf{m}_k - \mathbf{m}_{prior}) \end{bmatrix}. \quad (7)$$

In practice, \mathbf{m}_{prior} is often taken to be the model \mathbf{m}_k of the previous iteration, which helps convergence. This implies that, at the final tomography iteration, the prior tends to be equal to the maximum-likelihood model.

We emphasize that, in our implementation, all prior contributions to $\mathbf{C}_R^{1/2}$ are $N_M \times N_M$ square matrices. We do not use non-square matrices \mathbf{P} of size $p \times N_M$ with $p \ll N_M$ to parameterize constraints through $\mathbf{P}^\dagger \mathbf{P}$ ($\text{rank}(\mathbf{P}^\dagger \mathbf{P}) \leq p \ll N_M$). In other words, we do not use low-rank prior constraints that would reduce the dimensionality of the problem, such as steering filters [Clapp et al., 1998]. Our basis is a cardinal cubic bspline one, which is less constraining than steering filters. This gives more flexibility to “let the data talk” and makes it possible to avoid biased uncertainty analysis.

The physical dimensions of the components of \mathbf{A}_k are the inverse of the physical dimensions of the model. Thus, in the multi-kinds of parameter case (i.e. velocity with anisotropy), the coefficients of \mathbf{A}_k do not have the same physical dimensions. A preconditioning can be used:

$$\mathbf{A}'_k \rightarrow \mathbf{A}_k \mathbf{D}, \quad (8)$$

where \mathbf{D} is a square matrix that gives the same physical dimension and similar scaling to all coefficients of matrix $\mathbf{A}_k \mathbf{D}$ and can be used to re-weight \mathbf{A}_n to obtain better inversion results. \mathbf{D} is symmetric, $\mathbf{D}^\dagger = \mathbf{D}$, and should be invertible so that it does not increase the null space of the problem. A common preconditioning is to choose \mathbf{D} diagonal and put the inverse of the L_2 norm of each column of \mathbf{A}_k on the diagonal. We then solve, instead of equation 3,

$$\min_{\delta \mathbf{m}'_k} \|\mathbf{A}'_k \delta \mathbf{m}'_k - \mathbf{b}_k\|^2. \quad (9)$$

and recover $\Delta \mathbf{m}_k$ by

$$\delta \mathbf{m}_k = \mathbf{D} \delta \mathbf{m}'_k. \quad (10)$$

The solution of equation 9 is usually computed at each iteration using an approximation of $\delta \mathbf{m}'_k = \mathbf{A}_k'^{-g} \mathbf{b}_k$, where $\mathbf{A}_k'^{-g} = \lim_{\alpha \rightarrow 0^+} (\mathbf{A}_k'^\dagger \mathbf{A}'_k + \alpha \mathbf{I}_{N_M})^{-1} \mathbf{A}_k'^\dagger$ is the generalized (or Moore-Penrose pseudo-) inverse, where $\mathbf{A}_k'^\dagger \mathbf{A}'_k$ is called the Hessian matrix in the preconditioned domain. In our implementation, the Least-Squares Quadratic Relaxation (LSQR) algorithm is used to approximate the effect of $\mathbf{A}_k'^{-g}$ [Paige and Saunders, 1982, Choi, 2006].

LSQR and other iterative algorithms share a close similarity with performing a partial singular value decomposition (SVD) of \mathbf{A}'_k or a partial eigenvalue value decomposition

(EVD) of the Hessian $\mathbf{A}_k'^\dagger \mathbf{A}_k'$. LSQR needs some adaptations if we want to recover precisely the eigenvectors and eigenvalues [Zhang and Thurber, 2007]. Suppose that we perform $p \leq N_M$ iterations of SVD or EVD, each of them computing a new singular-value λ_i and its corresponding left and right eigenvectors \mathbf{u}_i and \mathbf{v}_i . We construct the $\mathbf{U}_p = [\mathbf{u}_1, \dots, \mathbf{u}_p]$ and $\mathbf{V}_p = [\mathbf{v}_1, \dots, \mathbf{v}_p]$ matrices, and the $p \times p$ matrix $\mathbf{\Lambda}_p^{1/2}$ that contains the singular values on its diagonal². The partial SVD of \mathbf{A}_n' gives the best possible rank p -approximation of \mathbf{A}_n'

$$\mathbf{A}_k' \approx \mathbf{U}_p \mathbf{\Lambda}_p^{1/2} \mathbf{V}_p^\dagger \Rightarrow \mathbf{A}_k'^{-g} \approx \mathbf{V}_p \mathbf{T}_p \mathbf{\Lambda}_p^{-1/2} \mathbf{U}_p^\dagger, \quad (11)$$

and the partial EVD of the Hessian is given by

$$\mathbf{A}_k'^\dagger \mathbf{A}_k' \approx \mathbf{V}_p \mathbf{\Lambda}_p \mathbf{V}_p^\dagger \Rightarrow (\mathbf{A}_k'^\dagger \mathbf{A}_k')^{-1} \approx \mathbf{A}_k'^{-g} \mathbf{A}_k'^{+g} \approx \mathbf{V}_p \mathbf{T}_p \mathbf{\Lambda}_p^{-1} \mathbf{V}_p^\dagger, \quad (12)$$

where

$$\mathbf{T}_p = [\mathbf{\Lambda}_p + \epsilon \mathbf{I}_p]^{-1} \mathbf{\Lambda}_p \quad (13)$$

is the Tikhonov regularization operator that stabilizes the inversion result in the event of very small components of $\mathbf{\Lambda}_p$ [Zhang and McMechan, 1995, Zhang and Thurber, 2007]. Note that this regularization is equivalent to including a “damping” level ϵ in a basis where all model components have the same units. In our case, we take $\epsilon = 0$ in \mathbf{T}_p as we already introduced a damping in our prior contributions, equation 6, that satisfies approximately $\mathbf{D}^{-1\dagger} \mathbf{D} \mathbf{amp}^\dagger \mathbf{D} \mathbf{amp} \mathbf{D}^{-1} \approx \epsilon \mathbf{I}_{N_M}$ in the preconditioned domain.

The $N_M - p$ eigenvectors not resolved by the iterative algorithms define the tomography “effective null space”, a cause of multiple equivalent effective solutions (depending among others on the initial model \mathbf{m}_0) and thus of uncertainty. The effective null space projector is [Munõz and Rath, 2006]

$$\mathbf{\Pi}_{null_p} = \mathbf{I}_{N_M} - \mathbf{V}_p \mathbf{V}_p^\dagger, \quad (14)$$

and the tomography “resolved” (or partial EVD spanned) space projector is³ [Munõz and Rath, 2006]

$$\mathbf{R}_p = \mathbf{V}_p \mathbf{V}_p^\dagger. \quad (15)$$

Bayesian formalism for tomography model uncertainties and migration structural uncertainties

At the last tomography iteration ($k = n$), the obtained \mathbf{m}_n is considered to be the maximum-likelihood solution. The result is uncertain because the tomography input data, modeling, and constraints contain uncertainties. As a basis for uncertainty considerations, we will use the Bayesian formalism. This gives a clear definition of uncertainties in terms of physics plus a confidence level, or probability P that the true model belongs to a region of the model space [Cowan, 1998]. This is important for reservoir risk analysis.

We consider, within Bayesian theory, the “Gaussian posterior pdf in the model space” corresponding to equation 1. It is defined up to a proportionality constant by [Tarantola, 2005]

$$\tilde{\rho}_M(\mathbf{m}) \propto \exp \left[-\frac{1}{2} (\mathbf{d}(\mathbf{m}) - \mathbf{d}_{obs})^\dagger \mathbf{C}_D^{-1} (\mathbf{d}(\mathbf{m}) - \mathbf{d}_{obs}) - \frac{1}{2} (\mathbf{m} - \mathbf{m}_{prior})^\dagger \mathbf{C}_M^{-1} (\mathbf{m} - \mathbf{m}_{prior}) \right]. \quad (16)$$

² \mathbf{U}_p has size $(N_D + L \times N_M) \times p$ and \mathbf{V}_p has size $N_M \times p$. Note that \mathbf{U}_p and \mathbf{V}_p are not unitary. They satisfy $\mathbf{V}_p^\dagger \mathbf{V}_p = \mathbf{U}_p^\dagger \mathbf{U}_p = \mathbf{I}_p$. But $\mathbf{V}_p \mathbf{V}_p^\dagger \neq \mathbf{I}_{N_M}$ for $p < N_M$, and $\mathbf{U}_p \mathbf{U}_p^\dagger \neq \mathbf{I}_{N_D + L \times N_M}$.

³ $\mathbf{R}_p \mathbf{\Pi}_{null_p} = \mathbf{\Pi}_{null_p} \mathbf{R}_p = \mathbf{I}_{N_M}$.

Take $\mathbf{m}_{\text{prior}} = \mathbf{m}_n$ in equation 16 (which implies that $\mathbf{m}_{\text{prior}}$ is chosen to be the previous iteration result, in agreement with most methods used to solve inverse problems, cf. section “Tomography inverse problem...”). Consider the first-order (linear) approximation

$$\mathbf{d}(\mathbf{m}) \approx \mathbf{G}_n(\mathbf{m} - \mathbf{m}_n) + \mathbf{d}(\mathbf{m}_n), \quad (17)$$

that holds in some region around \mathbf{m}_n (the weaker the non-linearity in $\mathbf{d}(\mathbf{m})$ the larger the region). Then, equation 16 can be rewritten as

$$\tilde{\rho}_M(\mathbf{m}) \propto \exp \left[-\frac{1}{2}(\mathbf{m} - \mathbf{m}_n)^\dagger \tilde{\mathbf{C}}_M^{-1}(\mathbf{m} - \mathbf{m}_n) \right], \quad (18)$$

where $\tilde{\mathbf{C}}_M$ denotes the “posterior” covariance matrix in the model space, defined through

$$\tilde{\mathbf{C}}_M^{-1} = \mathbf{G}_n^\dagger \mathbf{C}_D^{-1} \mathbf{G}_n + \mathbf{C}_M^{-1} = \mathbf{H}_n. \quad (19)$$

Its inverse \mathbf{H}_n is the posterior Hessian matrix. $\tilde{\rho}_M(\mathbf{m})$ gives information on the confidence region associated with a confidence level P (equal to the integral of $\tilde{\rho}_M(\mathbf{m})$ over the confidence region). The maximum-likelihood model \mathbf{m}_n does not represent the true model, but the most probable one according to the set of data and priors. Many other probabilistically pertinent models (or “admissible” model perturbations) exist. $\tilde{\rho}_M(\mathbf{m})$ allows a characterization of these models in terms of confidence levels, thus representing a key to extracting uncertainty information with a clear meaning.

Using notations of section “Tomography inverse problem...”, the posterior inverse covariance matrix, equation 19, can be also computed through

$$\tilde{\mathbf{C}}_M^{-1} = \mathbf{A}_n^\dagger \mathbf{A}_n = \mathbf{D}^{-1+} \mathbf{A}_n' \mathbf{A}_n' \mathbf{D}^{-1}. \quad (20)$$

The EVD of $\tilde{\mathbf{C}}_M$, also defined through the SVD of \mathbf{A}_n' , contains uncertainty information. Indeed, the principal axes of the Gaussian posterior pdf, equation 18, are given by the eigenvectors of $\tilde{\mathbf{C}}_M$ and the deformations of the pdf by the eigenvalues of $\tilde{\mathbf{C}}_M$. The “more extended” or poorly resolved directions correspond to smaller eigenvalues of $\tilde{\mathbf{C}}_M$.

We are interested in computing migration structural uncertainties on target reflectors, i.e. migration uncertainties related to the kinematic part of the Kirchhoff operator. Tomography model uncertainties represent a main contributor to migration kinematic uncertainties. We can therefore first generate admissible tomography model perturbations, i.e. perturbed models from equations 18 and 20. Then, migrations using each perturbed model can be performed and analyzed. A study of the results would allow us to estimate migration kinematic uncertainty-related quantities.

Full Kirchhoff migrations may be considered, but it is difficult to separate structural uncertainties from other uncertainties in migrated images, such as those related to amplitudes. [Li et al., 2014] propose to use the Euclidean and Procrustes distances to somewhat perform such a separation. Here, we are interested mostly in the structural uncertainties related to target reflectors, a crucial component of migration uncertainties. We consider a kinematic approximation of the Kirchhoff operator, called kinematic migration [Duffet and Sinoquet, 2006, Guillaume et al., 2008]. \mathbf{h} represents the result of the kinematic migration of an event (depth and slope of a reflector, etc.). We have

$$\mathbf{h} = \mathbf{k}(\mathbf{m}), \quad (21)$$

where $\mathbf{k}(\mathbf{m})$ is the kinematic migration operator for a given data (reflection event), non linear with respect to the tomography velocity \mathbf{m} . We compute the maximum-likelihood position of a target reflector \mathbf{h}_n related to the maximum-likelihood tomography model \mathbf{m}_n :

$$\mathbf{h}_n = \mathbf{k}(\mathbf{m}_n). \quad (22)$$

Let us consider a linearization of $\mathbf{k}(\mathbf{m})$ around \mathbf{m}_n :

$$\begin{aligned} (\mathbf{h} - \mathbf{h}_n) &\approx \mathbf{K}^\dagger(\mathbf{m} - \mathbf{m}_n) \\ \mathbf{K}^\dagger &= \left. \frac{\partial \mathbf{k}(\mathbf{m})}{\partial \mathbf{m}} \right|_{\mathbf{m}=\mathbf{m}_n}, \end{aligned} \quad (23)$$

where \mathbf{K} represents the linearized approximation (or Jacobian matrix) of the kinematic migration operator. The migration structural posterior covariance matrix related to \mathbf{h}_n is then defined through

$$\begin{aligned} \tilde{\mathbf{C}}_K^{-1} &= \mathbf{K}^\dagger \tilde{\mathbf{C}}_M^{-1} \mathbf{K}, \\ (\mathbf{h} - \mathbf{h}_n)^\dagger \tilde{\mathbf{C}}_K^{-1} (\mathbf{h} - \mathbf{h}_n) &\approx (\mathbf{m} - \mathbf{m}_n)^\dagger \tilde{\mathbf{C}}_M^{-1} (\mathbf{m} - \mathbf{m}_n). \end{aligned} \quad (24)$$

Using notation similar to equation 16, $\tilde{\mathbf{C}}_H$ defines the structural migration posterior pdf $\tilde{\rho}_H(\mathbf{h})$ in a similar way to equation 18, and contains information on migration structural uncertainties (related to the tomography model uncertainties). Map migrations (i.e. zero-offset kinematic migrations) of target reflectors are most often used in practice [Duffet and Sinoquet, 2006, Osypov et al., 2008b, Osypov et al., 2013, Messud et al., 2017b, Messud et al., 2017a]. Once a set of perturbed models $\{\mathbf{m}\}$ that follow equation 18 is generated (and possibly some spurious models removed), map migrations of target reflectors may be performed. This will give perturbed horizons $\{\mathbf{h}\}$ of target reflectors that will be related to the migration structural posterior pdf according to equation 24. Some statistical analysis allows us to deduce structural uncertainty quantities related to a target reflector and a given confidence level P [Duffet and Sinoquet, 2006, Osypov et al., 2008b, Osypov et al., 2013].

Note that, specific to our non-linear slope tomography, full kinematic migrations (using all offsets) of all the tomography data (invariants) can be considered. This makes it possible to deduce positioning uncertainty quantities in the whole migrated volume, not only at target reflector positions, which is an advantage over zero-offset computations.

Of course, the obtained uncertainties should be interpreted in the light of the tomographic data that have been used to compute them (for instance, if faults are not inverted by the tomography, uncertainties on faults cannot be handled by this method). Also, the method is valid if the linearization, equation 23, holds. But its range of validity should approximately be the same as that of the linearization which allowed us to define the tomography $\tilde{\mathbf{C}}_M$, equation 17, that is coherent. This will be further discussed below.

The main question now is: How to generate perturbed models from equation 18, together with a confidence level P ? We first review previous work in a unifying framework, then highlight open questions, and finally present our contribution.

Sampling a normal distribution to generate a set of perturbed tomography models

Suppose we can find a matrix \mathbf{E} that satisfies

$$\tilde{\mathbf{C}}_M^{-1} \approx \mathbf{E}^\dagger \mathbf{E} \quad \Rightarrow \quad \tilde{\mathbf{C}}_M \approx \mathbf{B} \mathbf{B}^\dagger \quad \text{where} \quad \mathbf{B} = \mathbf{E}^{-g}. \quad (25)$$

Then, the posterior pdf, equation 18, can be rewritten

$$\tilde{\rho}_M(\mathbf{m}) \propto \exp \left[-\frac{1}{2} \delta \mathbf{r}^\dagger \delta \mathbf{r} \right] \quad \text{where} \quad \delta \mathbf{r} = \mathbf{E} \Delta \mathbf{m}. \quad (26)$$

$\Delta \mathbf{m}$ represents perturbations of the maximum-likelihood model

$$\Delta \mathbf{m} = \mathbf{m} - \mathbf{m}_n. \quad (27)$$

Equation 26 implies that the covariance matrix associated with the vector $\delta\mathbf{r}$ is the identity \mathbf{I} , i.e. that the $\delta\mathbf{r}$ coordinates are not correlated and all have a variance of 1. One method of generating tomography model perturbations $\Delta\mathbf{m}$ that follow the Gaussian distribution 18 is to draw $\delta\mathbf{r}$ from a normal distribution $\mathcal{N}(\mathbf{0}, \mathbf{I})$ and compute

$$\Delta\mathbf{m} = \mathbf{B}\delta\mathbf{r}, \quad (28)$$

where \mathbf{B} is a matrix that contains the posterior covariance information and scaling. Once a set of perturbed models $\{\Delta\mathbf{m} + \mathbf{m}_n\}$ is generated (and possibly some spurious models discarded), migration structural or kinematic uncertainty quantities can be deduced using the method presented above. We now discuss possible choices for \mathbf{B} and corresponding dimensionality. The next three sections describe existing methods and their limitations, and underline questions still to be clarified. Then, the rest of the article presents our method.

Cholesky decomposition and partial SVD-based methods

Suppose we have computed $\tilde{\mathbf{C}}_M^{-1} = \mathbf{A}_n^\dagger \mathbf{A}_n$. [Duffet and Sinoquet, 2006] propose to perform a Cholesky decomposition of $\tilde{\mathbf{C}}_M^{-1}$. This implies finding a lower-triangular square matrix \mathbf{E} of size $N_M \times N_M$ that satisfies (exactly) equation 25 and computing (\mathbf{E} being invertible as $\tilde{\mathbf{C}}_M^{-1}$ is)

$$\mathbf{B} = \mathbf{E}^{-1}, \quad (29)$$

to generate model perturbations using equation 28. \mathbf{B} is a matrix of size $N_M \times N_M$ and $\delta\mathbf{r}$ is a vector of size N_M draw from $\mathcal{N}(\mathbf{0}, \mathbf{I}_{N_M})$. This scheme is costly and may lose accuracy if \mathbf{A}_n is ill-conditioned [Zhang and Thurber, 2007].

Another method is to use a partial SVD of \mathbf{A}_n' , equation 11. With equations 20 and 25, we deduce

$$\mathbf{E} = \mathbf{\Lambda}_p^{1/2} \mathbf{V}_p^\dagger \mathbf{D}^{-1} \Rightarrow \mathbf{B} = \mathbf{E}^{-g} = \mathbf{D} \mathbf{V}_p \mathbf{T}_p^{1/2} \mathbf{\Lambda}_p^{-1/2}, \quad (30)$$

where Tikhonov regularization has been added for the generalized inverse computation. \mathbf{B} is a matrix of size $N_M \times p$ and $\delta\mathbf{r}$ a vector of size p , denoted by $\delta\mathbf{p}$ to make the size explicit and draw from $\mathcal{N}(\mathbf{0}, \mathbf{I}_p)$. This scheme reduces the space of model perturbations, usually to the degrees of freedom that can be resolved by tomography, which is numerically advantageous but implies an SVD-based low-rank approximation. (We did not find applications of this scheme in the literature.)

Prior-based low-rank decomposition method

This section details the formalism of [Osypov et al., 2013, Osypov et al., 2011, Osypov et al., 2008a] and the specific form obtained for \mathbf{B} . Let us consider prior contributions to the prior covariance matrix in equation (31), that are not represented by square matrices of size $N_M \times N_M$ but by a non-square matrix \mathbf{P} of size $N_M \times p$ with $p < N_M$

$$\mathbf{C}_M \rightarrow \mathbf{P}\mathbf{P}^\dagger. \quad (31)$$

As $p \ll N_M$ is chosen in practice, low-rank prior constraints are considered, unlike in section ‘‘Tomography inverse problem...’’ and equation 6. The obtained \mathbf{C}_M in equation 31 is not strictly invertible, i.e. not strictly speaking a covariance matrix (even if the generalized inverse can be defined). \mathbf{P} can for instance be a steering filter that contains

information on the structures, allowing us to reduce the dimensionality of the problem ($p \ll N_M$) [Clapp et al., 1998]. \mathbf{P} is called a preconditioner in [Osypov et al., 2013, Osypov et al., 2011, Osypov et al., 2008a], but it has a very different role from our preconditioner \mathbf{D} introduced in section “Tomography inverse problem...”. We thus here call it “model preconditioner”.

Gathering many constraints within this formalism is done in the model preconditioned basis (note that $\mathbf{C}_R^{1/2}$ is considered contrarywise to equation 6 that considers $\mathbf{C}_R^{-1/2}$)

$$\begin{aligned}\mathbf{C}_R^{1/2} &= [\mathbf{P}\mathbf{Q}_1, \text{etc. } \mathbf{P}\mathbf{Q}_L] \\ \mathbf{C}_M &= \mathbf{C}_R^{1/2} \mathbf{C}_R^{1/2\dagger} = \mathbf{P} \left(\sum_{i=1}^L \mathbf{Q}_i^\dagger \mathbf{Q}_i \right) \mathbf{P}^\dagger,\end{aligned}\tag{32}$$

where \mathbf{Q}_i is a $p \times p$ matrix that can for instance contain the coupling between the various model contributions or subsurface parameters in the anisotropic case [Osypov et al., 2013, Osypov et al., 2011, Osypov et al., 2008a]. To lighten the notations, we do not consider such additional constraints in the following.

We have, using the generalized inverse

$$\tilde{\mathbf{C}}_M \approx [\mathbf{G}_n^\dagger \mathbf{C}_D^{-1} \mathbf{G}_n + (\mathbf{P}\mathbf{P}^\dagger)^{-g}]^{-g} = \mathbf{P} [(\mathbf{G}_n \mathbf{P})^\dagger \mathbf{C}_D^{-1} (\mathbf{G}_n \mathbf{P}) + \mathbf{I}_p]^{-1} \mathbf{P}^\dagger,\tag{33}$$

where $(\mathbf{G}_n \mathbf{P})^\dagger \mathbf{C}_D^{-1} (\mathbf{G}_n \mathbf{P}) + \mathbf{I}_p$ is a $p \times p$ matrix that is invertible because it is positive definite (\mathbf{I}_p kills the null eigenvalues). Now, let us perform the following partial EVD with $q \leq p$ iterations (no additional preconditioning is needed as the matrices are dimensionless and the problem is well conditioned in the model preconditioned domain)

$$(\mathbf{G}_n \mathbf{P})^\dagger \mathbf{C}_D^{-1} (\mathbf{G}_n \mathbf{P}) \approx \mathbf{V}_q \mathbf{\Lambda}_q \mathbf{V}_q^\dagger.\tag{34}$$

We deduce

$$\tilde{\mathbf{C}}_M \approx \mathbf{P} [\mathbf{V}_q \mathbf{\Lambda}_q \mathbf{V}_q^\dagger + \mathbf{I}_p]^{-1} \mathbf{P}^\dagger.\tag{35}$$

The binomial inverse theorem recalled in Appendix A leads to

$$\tilde{\mathbf{C}}_M \approx \mathbf{P} [\mathbf{I}_p - \mathbf{V}_q \mathbf{V}_q^\dagger + \mathbf{V}_q (\mathbf{\Lambda}_q + \mathbf{I}_q)^{-1} \mathbf{V}_q^\dagger] \mathbf{P}^\dagger.\tag{36}$$

Using equation 25, we finally obtain [Osypov et al., 2013, Osypov et al., 2011, Osypov et al., 2008a]

$$\mathbf{B} = \mathbf{P} [\mathbf{I}_p - \mathbf{V}_q \mathbf{V}_q^\dagger + \mathbf{V}_q (\mathbf{\Lambda}_q + \mathbf{I}_q)^{-1/2} \mathbf{V}_q^\dagger],\tag{37}$$

allowing us to generate perturbations in the model space by equation 28. As here $\delta \mathbf{r}$ is a vector of size $p \ll N_M$, we denote it by $\delta \mathbf{p}$ to make the size explicit. $\delta \mathbf{p}$ must be drawn from $\mathcal{N}(\mathbf{0}, \mathbf{I}_p)$. \mathbf{B} is a matrix of size $N_M \times p$ that can be split into

$$\begin{aligned}\mathbf{B} &= \mathbf{B}_q^{res} + \mathbf{B}_{q\%p}^{un-res} \\ \mathbf{B}_q^{res} &= \mathbf{P} \mathbf{V}_q (\mathbf{\Lambda}_q + \mathbf{I}_q)^{-1/2} \mathbf{V}_q^\dagger \\ \mathbf{B}_{q\%p}^{un-res} &= \mathbf{P} [\mathbf{I}_p - \mathbf{V}_q \mathbf{V}_q^\dagger] \\ \Delta \mathbf{m} &= \mathbf{B} \delta \mathbf{p} \quad \text{where} \quad \delta \mathbf{p} \sim \mathcal{N}(\mathbf{0}, \mathbf{I}_p),\end{aligned}\tag{38}$$

where two terms appear:

- \mathbf{B}_q^{res} deals with the uncertainty information contained in the posterior covariance matrix and resolved by the partial EVD. Indeed, $\mathbf{V}_q (\mathbf{\Lambda}_q + \mathbf{I}_q)^{-1/2} \mathbf{V}_q^\dagger$ represents the partial EVD of $\tilde{\mathbf{C}}_M^{1/2}$ in the model preconditioned domain.

- $\mathbf{B}_{q\%p}^{un-res}$ contains a projector on an effective null space of dimension $p - q$, as q EVD iterations have been used to approximate a $p \times p$ matrix. So, only the effective null space of the EVD in the model preconditioned domain (of size p) can be explored by this method. This is a very limited part of the full null space of the tomography operator (because $q \leq p \ll N_M$), producing only smooth perturbations. The advantage is that it allows us to explore some part of the effective null space of the EVD while keeping geological structures in the model perturbations (the perturbations are projected on \mathbf{P}).

Questions

The methods described in the previous two sections have limitations and raise questions. In particular, the following points still need to be clarified:

- A QC of the validity of the Gaussian and linearized hypothesis. This is fundamental to check if uncertainties obtained by our computations are pertinent. We propose a new sampling method that, together with non-linear slope tomography, will address this need, together with computational efficiency.
- Separation and exploration of the full effective null space of the tomography operator are not addressed by the previous methods, but this would certainly give interesting complementary uncertainty information (mainly relating to illumination issues, which are a major source of uncertainty). A simple way to explore a part of the tomography null space is to perform various tomographies with different priors and initial models, but this would be very costly numerically. In the following, we will propose a method within the linearized approximation, using the effective null space projector.
- A definition of error bars for the 68.3% confidence level, which accounts for the non-diagonal part of the covariance matrices (not only for the variances), will be given. This gives a more precise error bar evaluation (accounting only for variance underestimates the errors).
- Are the computed uncertainties quantitative or qualitative? We will extensively discuss this point.

Our first new contribution: Sampling a Gaussian equi-probable contour to generate a set of perturbed tomography models

Let us return to the tomography posterior Gaussian pdf, equation 18, and propose a different sampling method that will reduce the sampled space and thus optimize the exploration. We consider an equi-probable contour

$$\Delta \mathbf{m}^\dagger \tilde{\mathbf{C}}_M^{-1} \Delta \mathbf{m} = Q_{N_M}(P), \quad (39)$$

where $Q_{N_M}(P)$ is the quantile of order P of the Chi-square distribution [Cowan, 1998] (this distribution is among others used in confidence interval estimations related to Gaussian random variables).

Resolving (or sampling) equation 39 for a given P value gives the set of maximum perturbations (or the boundary of the confidence region) associated with a confidence level P ; Figure 1 gives an illustration. The probability that the true model \mathbf{m} lies within the N_M -dimensional hyper-ellipsoid of center \mathbf{m}_n defined by equation 39 is equal to P . Restricting the sampled space to an equi-probable contour does not hamper the assessment of the

uncertainties compared to the sampling of the full pdf because information on the full Gaussian is contained in one contour and the corresponding P value. Indeed, all hyper-ellipsoids defined by equation 39 are related by a simple proportionality constant.

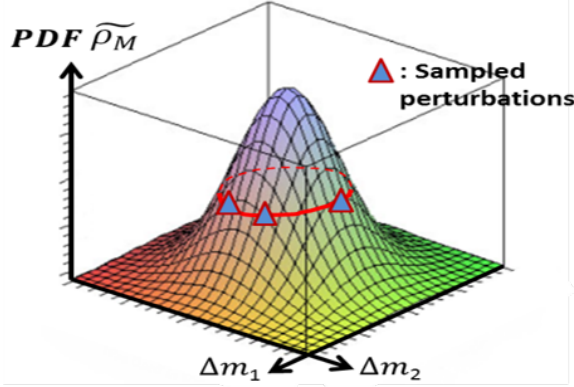


Figure 1: Equi-probable contour of a posterior Gaussian pdf ($N_M = 2$) (red) and $\Delta \mathbf{m}$ samples (triangles).

In the following, we consider a confidence level $P = 68.3\%$. We call it the standard-deviation-like confidence level [Messud et al., 2017a] because it corresponds to a standard deviation interval when $N_M = 1$ or when model parameters are non-correlated and their single pdfs are considered independently, see Appendix B. For more generality, we define uncertainties through the tomography confidence region related to a probability $P = 68.3\%$ and resolve equation 39 to generate a set of admissible perturbations. In the spirit of the considerations of section “Sampling a normal distribution...”, the solution is

$$\delta \mathbf{r}^\dagger \delta \mathbf{r} = Q_{N_M}(68.3\%) \quad \text{and} \quad \tilde{\mathbf{C}}_M \approx \mathbf{B} \mathbf{B}^\dagger \Rightarrow \Delta \mathbf{m} = \mathbf{B} \delta \mathbf{r}, \quad (40)$$

where $\delta \mathbf{r}$ is a vector of size N_M drawn from a uniform distribution and rescaled to have norm $\|\delta \mathbf{r}\|_2 = \sqrt{Q_{N_M}(68.3\%)}$ (it must not be drawn from a Gaussian distribution here, as we sample only an equi-probable contour). In our case, \mathbf{B} will be a $N_M \times N_M$ matrix as we do not use low-rank prior constraints that reduce the dimensionality of the problem. This gives more flexibility and avoids curbing a priori the uncertainty analysis.

Generating model perturbations from an equi-probable contour sampling has the advantage of reducing the sampled space to its most representative components, optimizing the computation compared to the previously described methods where the full pdf had to be sampled. This allows us to obtain stable error bars with 200-500 random models, without introducing any preconditioning that would reduce the dimensionality of the model space, as described further.

Let us now specify a problem concerning error bars. Why not simply define error bars by $\pm \sqrt{\text{diag}(\tilde{\mathbf{C}}_M)}$, where $\text{diag}(\tilde{\mathbf{C}}_M)$ denotes the vector containing the diagonal elements of $\tilde{\mathbf{C}}_M$? This is sometimes used as a first tomography model uncertainty indicator [Osypov et al., 2013], but it has pathologies. When $\tilde{\mathbf{C}}_M$ is diagonal, a subset of the solutions of equation 39 with $P = 68.3\%$ is

$$\Delta \mathbf{m} = \pm \sqrt{\frac{Q_{N_M}(68.3\%)}{N_M}} \sqrt{\text{diag}(\tilde{\mathbf{C}}_M)}, \quad (41)$$

defining a confidence interval. So, firstly, using equation 41 would be better than using $\pm \sqrt{\text{diag}(\tilde{\mathbf{C}}_M)}$ from a confidence level point of view (indeed, $\pm \sqrt{\text{diag}(\tilde{\mathbf{C}}_M)}$ is not associated with a constant confidence level $P = 68.3\%$ as N_M varies). However, equation 41 is still too restrictive, since:

- Even in the diagonal case, the full solution of equation 39 with $P = 68.3\%$ defines a larger (hyper-ellipsoidal) confidence region, encompassing the confidence interval defined by equation 41. So, equation 41 underestimates uncertainties.
- In the general case, $\text{diag}(\tilde{\mathbf{C}}_M)$ is not sufficient to generate a set of admissible tomography models. Indeed, non-diagonal elements of $\tilde{\mathbf{C}}_M$ can have a strong contribution as they describe correlations between model space nodes, which are crucial in tomography (because of the smoothness, structural conformity, etc. constraints on the model) [Duffet and Sinoquet, 2006]. Appendix B gives more formal details.

So, equation 40 must be resolved to represent the full solution of equation 39. It remains to define the \mathbf{B} matrix and how to compute exhaustive error bars from the equi-probable contour sampling.

Our second new contribution: Resolved and total space uncertainties

We consider an EVD of $\tilde{\mathbf{C}}_M^{-1}$ in the preconditioned domain (related to an SVD of \mathbf{A}'_n in the spirit of section “Tomography inverse problem...”)

$$\begin{aligned} \mathbf{D}^\dagger \tilde{\mathbf{C}}_M^{-1} \mathbf{D} &= \mathbf{V}_p \mathbf{\Lambda}_p \mathbf{V}_p^\dagger + \mathbf{V}_{N_M-p} \mathbf{\Lambda}_{N_M-p} \mathbf{V}_{N_M-p}^\dagger \\ &\approx \mathbf{V}_p \mathbf{\Lambda}_p \mathbf{V}_p^\dagger + \epsilon \mathbf{I}_{N_M}. \end{aligned} \quad (42)$$

$\mathbf{\Lambda}_{N_M-p} \rightarrow \epsilon \mathbf{I}_{N_M-p}$
 ϵ being the noise level

The second line shares similarity with a damping and is related to the noise-contaminated effective null space of the tomography. Equation 42 is a partial EVD of $\tilde{\mathbf{C}}_M^{-1}$ in the preconditioned domain (all model components or parameters have the same units in this domain), stopped after p iterations when the eigenvalues have reached a fixed prior level ϵ [Zhang and McMechan, 1995], and approximate the effect of the $N_M - p$ non-computed eigenvectors by $\epsilon \mathbf{I}_{N_M}$. In our applications, the damping level ϵ is fixed a priori and is selected sufficiently small so as not to affect the relevant information in the tomography operator, i.e. to be representative of the tomography noise level. The partial EVD is stopped when the eigenvalues have reached the damping level (another method would be to define the optimum p by eigenvalue decay and then deduce the corresponding ϵ ; because of our implementation in the preconditioned domain we do not need this). Using the binomial inverse theorem, Appendix A, we obtain

$$\begin{aligned} \tilde{\mathbf{C}}_M &\approx \mathbf{D} \left[\mathbf{V}_p \mathbf{\Lambda}_p \mathbf{V}_p^\dagger + \epsilon \mathbf{I}_{N_M} \right]^{-1} \mathbf{D}^\dagger \\ &= \mathbf{D} \left[\mathbf{V}_p \left(\mathbf{\Lambda}_p + \epsilon \mathbf{I}_p \right)^{-1} \mathbf{V}_p^\dagger + \frac{1}{\epsilon} \mathbf{\Pi}_{null_p} \right] \mathbf{D}^\dagger, \end{aligned} \quad (43)$$

where $\mathbf{\Pi}_{null_p}$ is the effective null space (dimension $N_M - p$) projector, see section “Tomography inverse problem...”. Using equation 40, we can compute

$$\mathbf{B} = \mathbf{D} \left[\mathbf{V}_p \left(\mathbf{\Lambda}_p + \epsilon \mathbf{I}_p \right)^{-1/2} \mathbf{V}_p^\dagger + \frac{1}{\sqrt{\epsilon}} \mathbf{\Pi}_{null_p} \right], \quad (44)$$

which can be split into

$$\begin{aligned} \mathbf{B} &= \mathbf{B}_p^{\text{resolved}} \mathbf{V}_p^\dagger + \mathbf{B}_{p\%N_M}^{\text{un-resolved}} \\ \mathbf{B}_p^{\text{resolved}} &= \mathbf{D} \mathbf{V}_p \left(\mathbf{\Lambda}_p + \epsilon \mathbf{I}_p \right)^{-1/2} \end{aligned} \quad (45)$$

$$\mathbf{B}_{p\%N_M}^{un-resolved} = \frac{1}{\sqrt{\epsilon}} \mathbf{D} \mathbf{\Pi}_{null_p}$$

$\Delta \mathbf{m} = \mathbf{B} \delta \mathbf{r}$ where $\delta \mathbf{r}$ is drawn from a uniform distribution

and rescaled to have norm $\sqrt{Q_{N_M}} (68.3\%)$.

Our method allows us to separate the following two uncertainty contributions:

- $\mathbf{B}_p^{resolved}$ deals with the uncertainty information contained in the posterior covariance matrix. It drives the contribution to $\Delta \mathbf{m}$ of the eigenvectors with eigenvalues above the prior damping level ϵ , which span the so-called tomography “resolved” space (of dimension p). As those eigenvectors are greatly constrained by the tomography input data, so are the related perturbations

$$\Delta \mathbf{m}^{resolved} = \mathbf{B}_p^{resolved} \delta \mathbf{p} \quad \text{where} \quad \delta \mathbf{p} = \mathbf{V}_p^\dagger \delta \mathbf{r} \text{ is a vector of size } p. \quad (46)$$

The perturbations tend to be structurally consistent and smooth (because tomography resolves the large wavelengths of the velocity model), as illustrated in Figure 2. They can be explored independently.

- $\mathbf{B}_{p\%N_M}^{un-resolved}$ contains the tomography full effective null space (of dimension $p - N_M$) projector. It drives the contribution in the uncertainties of eigenvectors with eigenvalues below ϵ , which span the tomography “unresolved space”. This space represents the full effective null space of tomography, constrained only by the regularizations and not by the input data. The related perturbations

$$\Delta \mathbf{m}^{un-resolved} = \mathbf{B}_{p\%N_M}^{un-resolved} \delta \mathbf{r}, \quad (47)$$

are obviously much less structurally consistent, but are nevertheless interesting. They give exhaustive information focused on what tomography cannot resolve, mainly related to illumination issues, which is an important source of uncertainty. One originality of the method presented here is to give also access to this contribution. Note that an explicit orthonormalization of the eigenvectors (like a Gram-Schmidt) can be numerically important [Zhang and Thurber, 2007], especially if we deal with the null space, for an accurate computation of $\mathbf{\Pi}_{null_p}$.

“Total” perturbations are given by the sum of both contributions,

$$\Delta \mathbf{m} = \Delta \mathbf{m}^{resolved} + \Delta \mathbf{m}^{un-resolved}, \quad (48)$$

with an example in Figure 2. The resolved space perturbation looks more organized, smoother and more correlated to structures and the tomography final model than the total perturbation. The total perturbation looks more random and of higher frequency, mainly because the tomography unresolved space is large and thus a dominant contributor to the total perturbation (i.e. the magnitude of $\Delta \mathbf{m}^{un-resolved}$ is larger than the magnitude of $\Delta \mathbf{m}^{resolved}$, approximately four times in this example). As will be illustrated further, this gives complementary information on the migration structural uncertainties, i.e. on the independent study of the $\Delta \mathbf{m}^{resolved}$ contribution.

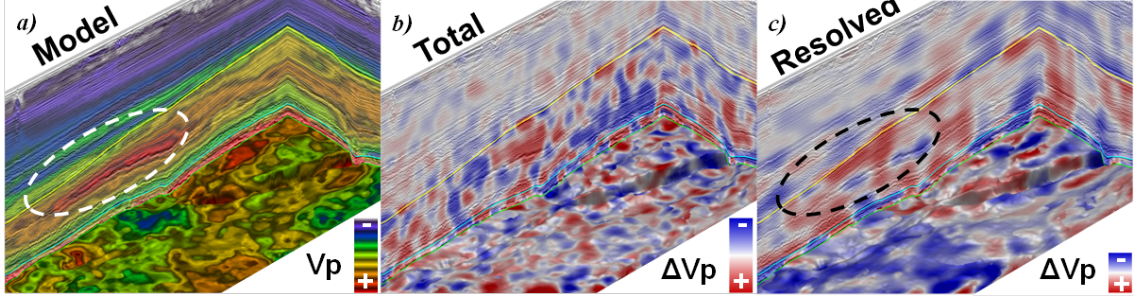


Figure 2: Left: Maximum-likelihood velocity (V_p) model \mathbf{m}_n . Perturbations $\Delta\mathbf{m}$ displayed on sections and one horizon; Middle: Total space; Right: Resolved space. From [Messud et al., 2018].

Using notations of § and equation 40 we have

$$\begin{aligned} \delta\mathbf{r} = \mathbf{R}_p\delta\mathbf{r} + \mathbf{\Pi}_{null_p}\delta\mathbf{r} &\Rightarrow \delta\mathbf{r}^\dagger\delta\mathbf{r} = \delta\mathbf{r}^\dagger\mathbf{R}_p\delta\mathbf{r} + \delta\mathbf{r}^\dagger\mathbf{\Pi}_{null_p}\delta\mathbf{r} \\ &= \delta\mathbf{p}^\dagger\delta\mathbf{p} + \delta\mathbf{r}^\dagger\mathbf{\Pi}_{null_p}\delta\mathbf{r} = Q_{N_M}(68.3\%), \end{aligned} \quad (49)$$

where the vector $\delta\mathbf{p}$ of dimension p is related to the projection of $\delta\mathbf{r}$ on the resolved subspace, equation 46. In the large N_M case (like in tomography), where $Q_{N_M}(68.3\%)$ remains close to N_M , one may think that equation 49 implies $\delta\mathbf{p}^\dagger\delta\mathbf{p} = p$ and $\delta\mathbf{r}^\dagger\mathbf{\Pi}_{null_p}\delta\mathbf{r} = N_M - p$, which would slightly simplify the problem. But this is not the case as amplitudes of the perturbations in resolved and unresolved subspaces are not fully independent from the total uncertainty point of view. Even if this may be true on average, an advantage of considering random perturbations $\delta\mathbf{r}$ of dimension N_M and projecting them on \mathbf{V}_p^\dagger to compute the p -dimensional perturbations $\delta\mathbf{p} = \mathbf{V}_p^\dagger\delta\mathbf{r}$ is that the latter will account for the structures (geology, etc.) in the eigenvectors.

Despite the formal similarities between our decomposition, equation 45, and the decomposition of “Prior based low-rank decomposition...”, equation 38, the content is different.

- In equation 38, \mathbf{B} is a $N_M \times p$ matrix and $\delta\mathbf{p}$ a p size vector, whereas in our case \mathbf{B} is a $N_M \times N_M$ matrix and $\delta\mathbf{r}$ a N_M size vector.
- In equation 38, tomography constraints are contained in the model preconditioner \mathbf{P} (a steering filter) through equation 31, whereas in our case the tomography constraints are contained in the eigenvectors and the illumination information in the preconditioner \mathbf{D} . This gives more flexibility to “let the data talk” and reduces the bias in the uncertainty analysis.
- In equation 38, there is no contribution similar to $\mathbf{B}_{p\%N_M}^{un-resolved}$, that describes the tomography full effective null space (dimension $p - N_M$). The $\mathbf{B}_{q\%p}^{un-res}$ of equation 38 describes the effective null space (dimension $p - q$) of the EVD in the model preconditioned domain, which is a very limited part of the full effective null space of the tomography operator (because $q \leq p \ll N_M$). If we consider that the p value in equation 45 is approximately the same as in equation 38, we can deduce a similarity between the two decompositions at the resolved space level:

$$\mathbf{B}_p^{resolved}\delta\mathbf{p} \approx (\mathbf{B}_q^{res} + \mathbf{B}_{q\%p}^{un-res})\delta\mathbf{p}, \quad (50)$$

where our $\delta\mathbf{p}$ is constrained to be equal to $\mathbf{V}_p^\dagger\delta\mathbf{r}$. The introduction of this constraint on $\delta\mathbf{p}$ and of the $\mathbf{B}_{p\%N_M}^{un-resolved}\delta\mathbf{r}$ term thus distinguishes our method. It allows us to split the uncertainty analysis into resolved and unresolved tomography spaces, that contain complementary information as illustrated further.

Our third new contribution: Exhaustive error bars

Uncertainty attributes can be computed statistically using the obtained set of perturbations for both resolved space, using the $\{\Delta \mathbf{m}^{resolved}\}$, and total space, using the $\{\Delta \mathbf{m}\}$:

- Tomography model 68.3% error bars on \mathbf{m}_n (velocity and anisotropy models):
Computed by considering the maximum possible variations of the model perturbations (i here represents the model grid coordinates):

$$\sigma_i^{(\mathbf{m}_n)} = \max\{\Delta m_i\}. \quad (51)$$

The true model belongs to $\mathbf{m}_n \pm \sigma^{(\mathbf{m}_n)}$ with a probability $P \geq 68.3\%$ [Messud et al., 2017a]. [Reinier et al., 2017] give an illustration of such error bars for the velocity and the total space.

- Maximum horizon perturbations within the 68.3% confidence region:
Kinematic or map migrations can be performed with each model perturbation to obtain a set of equi-probable horizon perturbations $\{\Delta \mathbf{h}\}$ around the maximum-likelihood horizon position \mathbf{h}_n . Note that those perturbations must not be interpreted as a migration pdf sampling, but as maximum possible perturbations within the 68.3% confidence region, cf. section “Bayesian formalism...” and particularly equation 24. They can be QCed, see Figure 3, and are used to compute horizon error bars (next item), but they should not be used as such in reservoir workflows that need perturbed horizons from a pdf sampling as an input (as the samples are not similar; they tend to be more concentrated around the maximum-likelihood for a pdf sampling). If needed, pdf sampling can easily be recovered from our equi-probable perturbations (a Gaussian pdf can easily be reconstructed from one of its equi-probable contours, cf. section “Sampling a Gaussian equi-probable contour...”).
- Horizon position 68.3% error bars:
A depth error bar can be defined as the maximum possible depth variation of the horizon perturbations (i here represents the horizon coordinates):

$$\sigma_i^{(\mathbf{h}_n)} = \max\{\Delta h_i\}. \quad (52)$$

Horizons move vertically and laterally for each map migration; $\sigma_i^{(\mathbf{h}_n)}$ considers the depth “envelope” of all migrated horizons and thus accounts for lateral displacements of migrated points. This gives 68.3% confidence level error-bars: the true horizon depth position belongs to $\mathbf{h}_n \pm \sigma^{(\mathbf{h}_n)}$ with a probability $P \geq 68.3\%$ [Messud et al., 2017a]. Lateral (x and y-directions) horizon error bars can be computed using the same principle, from differences of position between rays traced in \mathbf{m}_n and rays traced in the perturbed model.

Note that our error bars ($\sigma^{(\mathbf{m}_n)}$ and $\sigma^{(\mathbf{h}_n)}$) should not be computed from standard-deviations of the perturbations but from a maximum, as we sample a pdf equi-probable contour. They account for the non-diagonal elements of the tomography and migration posterior covariances, equations 19 and 24. Thus, they contain exhaustive uncertainty information, contrary to the diagonal elements of $\tilde{\mathbf{C}}_M$ and $\tilde{\mathbf{C}}_H$ (i.e. the variances). They therefore can be considered as “generalized standard deviations” and can be computed for the resolved and total spaces.

We emphasize again that the pdf equi-probable contour sampling has the advantage of reducing the sampled space to its most representative components, optimizing the error bar computation. We obtain stable error bars with 200-500 random models, without introducing any preconditioning that would reduce the dimensionality of the model space.

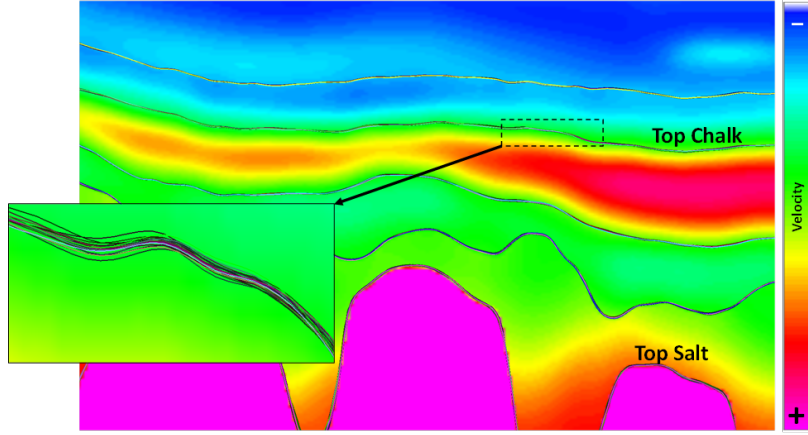


Figure 3: The maximum-likelihood prestack depth migration velocity model overlain with a subset of 20 (among several hundred) random migrated horizons from the perturbed models. From [Messud et al., 2017b].

Our fourth new contribution: Migration volumetric positioning error bars and QC of the Gaussian hypothesis (specific to non-linear slope tomography)

The use of a non-linear approach based on kinematic invariants, i.e. non-linear slope tomography [Guillaume et al., 2013b], also provides unique advantages:

- Firstly, as discussed in section “Bayesian formalism...”, full kinematic migrations (using all offsets) of the tomography data (invariant picks) can be performed on each model perturbation. Using the same “maximum” principle as in section “Exhaustive error bars...” allows us to deduce migration kinematic uncertainties in the whole migrated volume, not only at target reflector positions. This output is specific to our non-linear slope tomography and is called migration volumetric 68.3% error bars in the following.
- Non-linear slope tomography also provides an efficient way to assess the quality of the randomly generated model perturbations. Indeed, the cost functions related to the perturbations can be estimated automatically and non-linearly, allowing the consideration of some non-linear aspects of the problem. Combined with our posterior pdf equi-probable contour sampling, this allows us to QC the validity of the Gaussian hypothesis done in section “Bayesian formalism...”. This represents a strong advantage of our method. Figure 4 shows, for the first 46 perturbations, the non-linearly computed tomography cost functions (equal to equation 39 up to an additive constant in the linear approximation). It is obvious that almost iso-cost, i.e. equi-probable, $\delta\mathbf{m}$ were generated. We observe only limited variations around the average cost function value of the perturbed models, meaning that the linear hypothesis assumed in our analysis is appropriate. Interestingly, we see that no spurious perturbations related to too large variations of the cost function were generated. It is not necessary to have a step discarding spurious perturbations with our method (whereas it may be necessary with the method of section “Sampling a normal distribution...”).

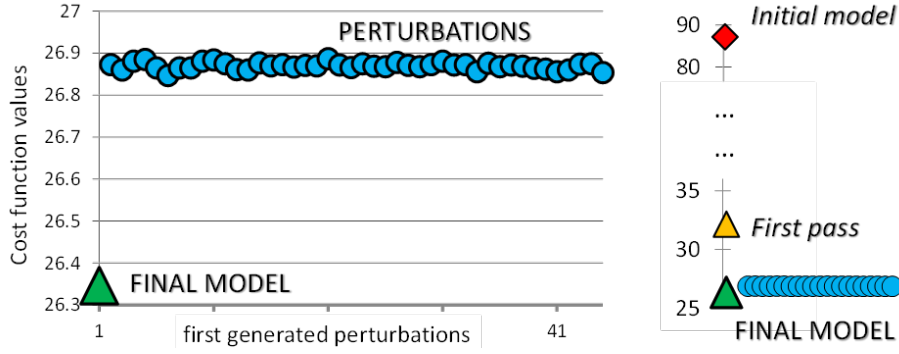


Figure 4: Left: Tomography cost function values for the final model (i.e. maximum-likelihood model) and the first 46 generated perturbed models among 500. Right: Cost function values after the velocity model building phases (first tomography pass and final tomography pass), represented with a larger nonlinear scale. From [Reinier et al., 2017].

Global proportionality constraint issue and error bar scaling

Many aspects that only slightly affect the maximum-likelihood search (i.e. the minimum of the cost function) may affect much more the uncertainty computation (i.e. the curvatures of the cost function at the minimum). Often overlooked, those aspects tend to affect uncertainties up to a global proportionality constant:

- Bayesian uncertainty reasoning holds strictly if the diagonals of \mathbf{C}_D (quality of the tomography picks) and \mathbf{C}_M (various model space constraints), that enter into $\tilde{\mathbf{C}}_M$ computation, represent variances, related to a confidence level of 68.3%. In practice, \mathbf{C}_D and \mathbf{C}_M tend to be defined up to a global proportionality constant, i.e. they are balanced together, so that they do not affect the maximum-likelihood. But the scaling of the global proportionality constant is not easy and itself uncertain.
- Data decimation will produce less “illumination” of each model node and therefore will tend to increase the uncertainties. Contrariwise, a larger model discretization step will produce more “illumination” of each model node and thus will tend to decrease the uncertainties. Those effects could theoretically be compensated by fine adaptation of the prior covariances, but this is not easy and basically requires knowledge of a large part of the inversion solution. Reasonable changes in data decimation and model discretization will tend to affect the uncertainties globally and linearly on average, i.e. up to a global proportionality constant.

The combination of those effects will tend to affect uncertainties approximately only up to a global proportionality constant (within equi-probable contour sampling as well as full pdf sampling). The global proportionality constant can be rescaled using posterior information external to the tomography, like wells. so that all well markers lie within the horizon error bars, see illustration in Figure 5. The resolved space error bars should be used for such a matching, as they contain the physical tomography information; after rescaling they become quantitative. The total error bars will remain qualitative (even after rescaling by the global constant found from the resolved space error bars) as null space exploration has been thresholded at the noise level ϵ . However, their hierarchy gives an interesting complementary uncertainty information as illustrated in the next section.

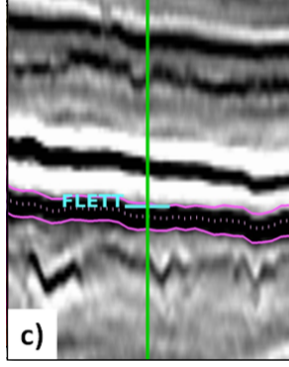


Figure 5: Zoom-in around one well with Base Flett marker (cyan), migrated image section, Base Flett horizon (pink dotted line) and horizon error bars (pink lines). From [Reinier et al., 2017].

Error bars illustrated on 3D field data

Let us illustrate our method on a first North Sea dataset merging four different overlapping narrow-azimuth towed-streamer surveys acquired over the years with different layout configurations. Figure 6a shows a compounded fold map of the surveys labelled A to D. The arrows indicate the different acquisition directions, and the overlapping parts with higher fold appear clearly. Figure 6b displays the computed total space depth error bars for the top chalk horizon. One can observe a clear correlation between the illumination map in Figure 6a and the total space depth error bars: the latter are smaller in overlap areas where the enlarged angle diversity (dip and azimuth) of raypaths improves the resolution of the tomographic operator. On the other hand, lower-fold areas such as the rig zone inside survey C show relatively higher total space error bars correlated with the poorer angle diversity of raypaths and the reduced illumination; we can also observe larger error bars on poorly illuminated survey edges. So, total space error bars highlight the combined effects of the acquisition fold and of the effective angle diversity that is in particular sensitive to structural complexities.

Figure 7 compares total and resolved space depth error bars. Again, total space error bars are dominated by the acquisition illumination variations (for instance, the narrow canyon in the middle is incompletely illuminated). The resolved space error bars give complementary information that tends to highlight how illumination diversity drives the discrimination power of the tomographic operator. The zoom in Figure 7 clearly shows larger resolved space depth error bars in steeply dipping parts of the top Chalk horizon located below velocity features in the overburden. One can observe the correlation between the velocity features in the overburden and the spatial distribution of the resolved space depth error bars at top chalk level. Also demonstrated in figure 4 of [Messud et al., 2017b], resolved space error bars correlate very well with steeply dipping flanks or faults, and are stronger when shooting and dipping/fault plane directions are parallel, thus confirming that shooting along the dip direction is better for resolution than shooting strike.

The hierarchy (or variation) of our error bars is thus related to the whole tomographic information: the changes in illumination, the distribution of angle and azimuth diversity, the spatial distribution of tomographic inversion data and the velocity complexity. The total space error bars are qualitative, cf. section “Global proportionality constraint issue...”, and more centered on the changes in illumination and the distribution of angle and azimuth diversity. The hierarchy gives complementary uncertainty information compared to resolved space error bars, which is more centered on the spatial distribution of tomographic inversion data and the velocity complexity.

In the examples above, horizon error bars were computed by (zero-offset) map migration in all model perturbations. However, as discussed in section “Migration volumetric positioning error bars...”, available tomographic picks (invariants) used by the non-linear slope tomography allow computing migration volumetric error bars by full kinematic migration (using all offsets) of the picks in all model realizations. Figure 8 shows an example of migration volumetric error bars for the resolved space, extracted on vertical sections and along a horizon. The error bars exhibit layered and velocity-correlated variations having longer spatial wavelengths as the full-offset range (not only zero-offset) is considered in the kinematic migrations. The advantage of the volumetric error bars is that they make it possible to track and understand the buildup of positioning uncertainties in the overburden and in-between horizons.

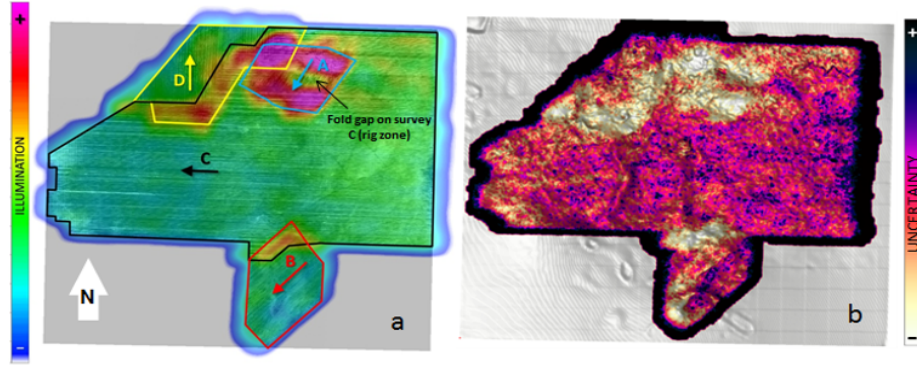


Figure 6: Top Chalk horizon attributes: (a) Illumination map with shooting direction of each survey indicated by the direction of the associated arrow and (b) total space horizon depth error bars. From [Messud et al., 2017a].

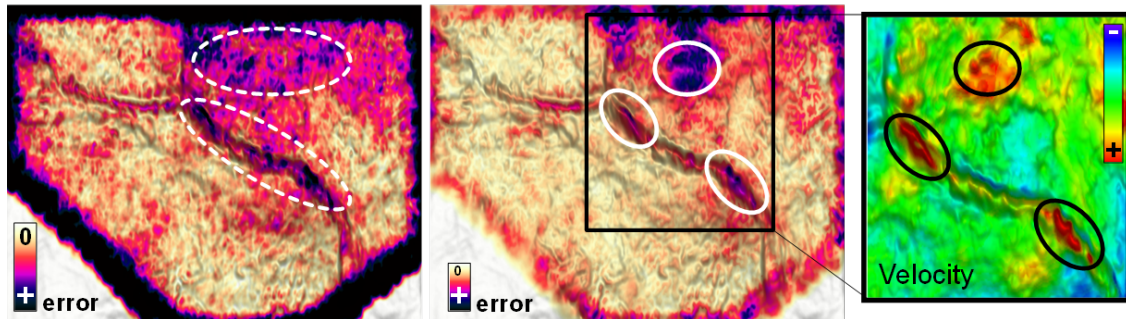


Figure 7: Horizon depth error bars. Left: Total space. Middle: Resolved space. Right: V_p extracted above the horizon. From [Messud et al., 2018].

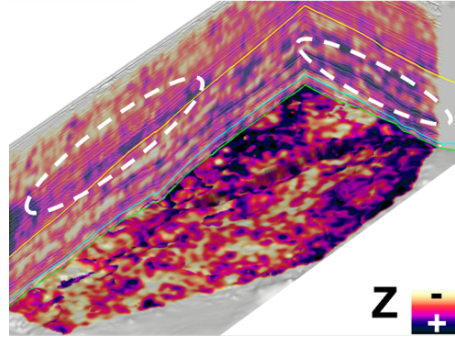
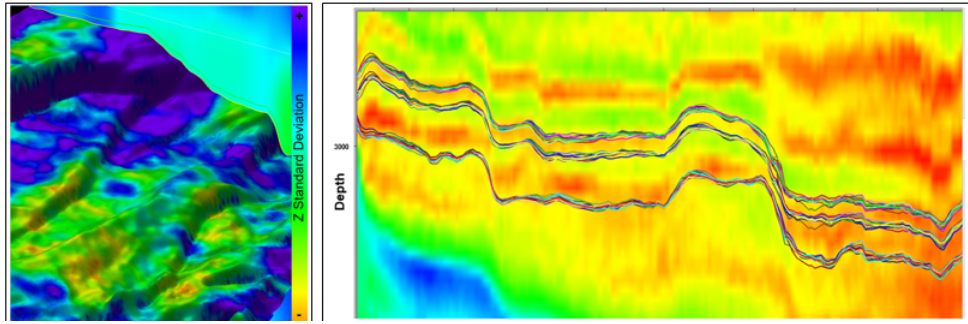
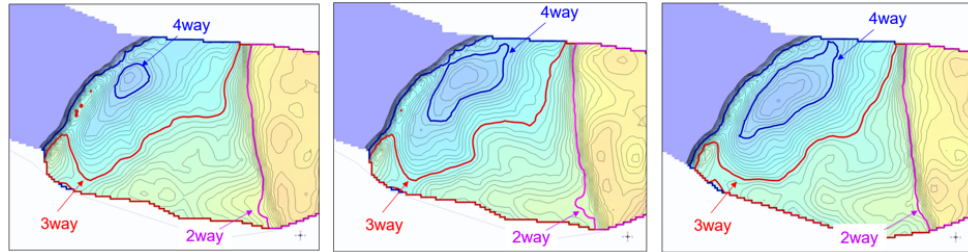


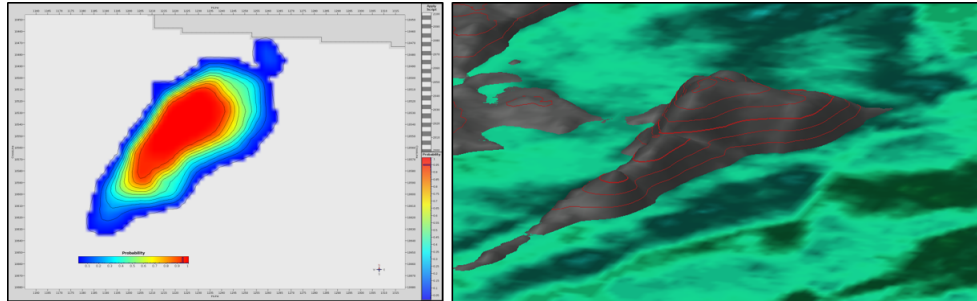
Figure 8: Migration volumetric depth error bars (resolved space), displayed on vertical sections and on a horizon.



(a) Left: Spatial variations of horizon depth error bars provide some assessment of the potential area with higher uncertainty. Right: display of desired number of realizations for some key horizons superimposed on velocity model attributes (estimated velocity parameters, error bars).



(b) Examples of reservoir contours for different spill point closure definitions and for different GRV scenarios (minimum case scenario on the left, average case in the center and maximum case on the right for the four-way closure type). For each scenario, the blue isoline represents the four-way closure, the red represents the three-way and the pink, the two-way closure.



(c) Left: Probability map finding closure above the spill point for multiple realizations. Right: One realization of a calibrated top reservoir surface.

Figure 9: Illustrating steps in GRV computation workflow and intermediate products or QCs. From [Coléou et al., 2019].

Let us now illustrate the integration of structural uncertainties into a downstream gross-rock volume (GRV) calculation workflow on a second seismic dataset. In a conventional stochastic approach, structural uncertainties are known at well locations and inferred elsewhere using variogram models. The presented tomography-based method allows more control between wells and provides a realization-based way of assessing the positioning of reservoir boundaries. Figure 9 illustrates key milestones in the workflow which breaks down as follows:

- Estimating the tomography maximum-likelihood velocity model and computing target horizon error bars tuned to observed mis-ties at some well locations (Figure 9a),
- For the Top and Base reservoir horizons, describing the channel system of interest, calibrating horizon realizations to well markers (Figure 9b). By doing so, uncertainties between wells are reflected by the spatial variations of horizon depth error bars derived from the tomographic operator.
- Estimating spill point depending on closure assumption for various horizon realizations. Figure 9b shows three fault-driven types of closure: “four-way” closure made of dip or channel limits, “three-way” and “two-way” closures add one or two sealed bounding faults.
- Calculating GRV from Base and Top reservoir down to spill point closure level, with all these elements being affected by the error bars in the migrated domain and along well paths.
- Assessing, for each identified prospect, the closure probability map made from all plausible horizon realizations and defining the chance of finding closure above the measured spill point. Figure 9c shows the probability map for one prospect, demonstrating the presence of robust structural closures in the same channel system.

This example emphasizes the importance of structural uncertainties for providing error bars between well locations and allowing the generation of corresponding horizon realizations.

Conclusion

The work presented by [Osypov et al., 2008a, Osypov et al., 2010, Osypov et al., 2011, Osypov et al., 2013] represents an important breakthrough for the industrial computation of migration structural uncertainties. This work provided a theoretical and numerical framework and has been applied to various E&P topics. Here we have proposed an extension of this work.

Firstly, we developed the application in the context of non-linear slope tomography. In addition to the advantages in terms of accuracy and efficiency of the VMB (compared to standard tomography) it provides the possibility to assess the quality of the linear and Gaussian assumptions. It also allows us to compute volumetric migration positioning error bars (using kinematic migration of each locally coherent event and not only map migration of horizons).

Secondly, we estimated error bars from the statistical analysis of perturbed models obtained from the sampling of an equi-probable contour of the posterior pdf (related to a clear confidence level), not of the full pdf as [Osypov et al., 2008a]. Thirdly, while Osypov et al. worked in a preconditioned model space (with a smaller dimensionality and where the prior model covariance is the identity matrix), we propose to work in the full model space, avoiding biased uncertainty analysis. We introduced the splitting of the full model space into resolved and unresolved spaces which allows characterization of both the contributions

of the data and regularizations, and of the null space. Fourthly, a general definition of error bars for a given confidence level was given.

Finally, all these concepts were illustrated on two field 3D datasets where emphasis was placed on the importance of horizon error bars, among others for GRV computation and uncertainty evaluation between well locations.

Our approach can easily apply to FWI-derived models. Indeed, state-of-the-art workflows involve interleaved FWI and tomography passes, ending with a tomography pass. The corresponding tomography uncertainty analysis can naturally be performed to produce an estimate for FWI model kinematic-related uncertainties.

Acknowledgments

The authors are particularly indebted to Mathieu Reinier, Hervé Prigent, Thierry Coléou, Jean-Luc Formento, Samuel Gray and Sylvain Masclet for collaboration and enlightening discussions. The authors are grateful to CGG for granting permission to publish this work. The authors thank PremierOil, Edison, Bayerngas, WesternGeco, INEOS, OMV and CGG Multi-Client & New Ventures Division for their permission to show the data. Figures 2 and 4-9 are courtesy of EAGE and figure 3 is courtesy of The Leading Edge.

A. The binomial inverse theorem and the Woodbury matrix identity

Consider an invertible (thus square) matrix \mathbf{A} of size $N \times N$. Consider a matrix \mathbf{V} of size $N \times K_1$, a matrix \mathbf{W} of size $K_1 \times K_2$, and a matrix \mathbf{U} of size $K_2 \times N$. If the square matrix $\mathbf{I}_{K_1} + \mathbf{U}\mathbf{A}^{-1}\mathbf{V}$ of size $K_1 \times K_1$ is invertible, we have the following identity, called binomial inverse theorem

$$(\mathbf{A} + \mathbf{V}\mathbf{U}\mathbf{W})^{-1} = \mathbf{A}^{-1} - \mathbf{A}^{-1}\mathbf{V}(\mathbf{I}_{K_1} + \mathbf{U}\mathbf{A}^{-1}\mathbf{V})^{-1}\mathbf{U}\mathbf{A}^{-1}. \quad (53)$$

If the matrix \mathbf{U} is invertible (thus square $K_1 = K_2 = K$), the previous expression can be reduced to the Woodbury matrix identity

$$(\mathbf{A} + \mathbf{V}\mathbf{U}\mathbf{W})^{-1} = \mathbf{A}^{-1} - \mathbf{A}^{-1}\mathbf{V}(\mathbf{U}^{-1} + \mathbf{W}\mathbf{A}^{-1}\mathbf{V})^{-1}\mathbf{W}\mathbf{A}^{-1}. \quad (54)$$

Consider $\mathbf{A} = \mathbf{I}_N$, \mathbf{U} square but not necessarily invertible, and $\mathbf{W} = \mathbf{V}^\dagger$ that satisfies $\mathbf{V}^\dagger\mathbf{V} = \mathbf{I}_K$. If the matrix $\mathbf{I}_K + \mathbf{U}$ is invertible, the binomial inverse theorem gives

$$(\mathbf{I}_N + \mathbf{V}\mathbf{U}\mathbf{V}^\dagger)^{-1} = \mathbf{I}_N - \mathbf{V}(\mathbf{I}_K + \mathbf{U})^{-1}\mathbf{U}\mathbf{V}^\dagger. \quad (55)$$

Using the binomial theorem again under same conditions, we obtain $(\mathbf{I}_K + \mathbf{U})^{-1}\mathbf{U} = \mathbf{I}_K - (\mathbf{I}_K + \mathbf{U})^{-1}$, and finally the following identity

$$(\mathbf{I}_N + \mathbf{V}\mathbf{U}\mathbf{V}^\dagger)^{-1} = \mathbf{I}_N - \mathbf{V}\mathbf{V}^\dagger + \mathbf{V}(\mathbf{I}_K + \mathbf{U})^{-1}\mathbf{V}^\dagger. \quad (56)$$

B. Standard-deviations and error bars

The multi-dimensional Gaussian posterior pdf, equation 18, can be rewritten (we do not consider the normalization factor here to simplify the notations without loss of generality, so that the maximum of the pdf is always 1)

$$\tilde{\rho}_M(\Delta\mathbf{m}) = \exp \left[-\frac{1}{2}\Delta\mathbf{m}^\dagger \tilde{\mathbf{C}}_M^{-1} \Delta\mathbf{m} \right] \quad (57)$$

$$= \prod_{i=1}^{N_M} \tilde{\rho}_{M_i}(\Delta \mathbf{m}),$$

where the posterior pdf for one model space node i is defined by

$$\begin{aligned} \tilde{\rho}_{M_i}(\Delta \mathbf{m}) &= \exp \left[-\frac{1}{2} \tilde{C}_{M_{ii}}^{-1} \Delta m_i^2 \right] \exp \left[-\frac{1}{2} A_i(\Delta \mathbf{m}) \Delta m_i \right] \\ A_i(\Delta \mathbf{m}) &= \sum_{\substack{j=1 \\ j \neq i}}^{N_M} \tilde{C}_{M_{ij}}^{-1} \Delta m_j. \end{aligned} \quad (58)$$

$A_i(\Delta \mathbf{m}) \Delta m_i$ may be negative and can be neglected only when the correlations $\tilde{C}_{M_{i,j \neq i}}^{-1}$ are sufficiently small.

Consider the models related to a given value $a \in [0, 1]$ of the un-normalized posterior pdf for one model space node, i.e. $\forall i = 1..N_M : \tilde{\rho}_{M_i}(\Delta \mathbf{m}) = a$. In other terms, a denotes a percentage of the maximum of each $\tilde{\rho}_{M_i}$. Using equation 57, this leads to

$$\begin{aligned} \tilde{\rho}_M(\Delta \mathbf{m}) &= a^{N_M}, \\ \Delta \mathbf{m}^\dagger \tilde{\mathbf{C}}_M^{-1} \Delta \mathbf{m} &= 2 \ln(1/a) \times N_M. \end{aligned} \quad (59)$$

This equation defines the set of model perturbations $\Delta \mathbf{m}$ related to a chosen a value for the posterior pdfs of each model space node $\tilde{\rho}_{M_i}(\Delta \mathbf{m})$. Equation 59 is equivalent to

$$\sum_{i=1}^{N_M} \tilde{C}_{M_{ii}}^{-1} \Delta m_i^2 + \sum_{i=1}^{N_M} A_i(\Delta \mathbf{m}) \Delta m_i = 2 \ln(1/a) \times N_M. \quad (60)$$

In the general case, one has to resolve the full equation 60 to obtain the solutions Δm_i . But if $|\sum_{i=1}^{N_M} A_i(\Delta \mathbf{m}) \Delta m_i| \ll |\sum_{i=1}^{N_M} \tilde{C}_{M_{ii}}^{-1} \Delta m_i^2|$, the solutions become

$$\Delta m_i = \pm \tilde{C}_{M_{ii}}^{1/2} \sqrt{2 \ln(1/a)}, \quad (61)$$

i.e. error bars are then related to the posterior standard deviations $\tilde{C}_{M_{ii}}^{1/2}$. Error bars become equal to $\pm \tilde{C}_{M_{ii}}^{1/2}$ if we select $a = 0.6$, that is related to a confidence probability $P(a) = 68.3\%$ (computing the correctly normalized integral of $\tilde{\rho}_M(\Delta \mathbf{m})$ inside the corresponding hyper-ellipsoid).

References

- [Adler et al., 2008] Adler, F., Baina, R., Soudani, M. A., Cardon, P., and Richard, J.-B. (2008). Nonlinear 3d tomographic least-squares inversion of residual moveout in kirchhoff prestack-depth-migration common image gathers. *Geophysics*, 73(5):VE2–VE13.
- [Al Chalabi, 1994] Al Chalabi, M. (1994). Seismic velocities, a critique. *First Break*, 12(12):589–596.
- [Allemand et al., 2017] Allemand, T., Sedova, A., and Hermant, O. (2017). Flattening common image gathers after full-waveform inversion: the challenge of anisotropy estimation. *87th SEG Annual Meeting, Expanded Abstracts*, pages 1410–1415.
- [Choi, 2006] Choi, S.-C. (2006). *Iterative methods for singular linear equations and least-squares problems*. PhD thesis, Stanford University.

- [Clapp et al., 1998] Clapp, R. G., Biondi, B. L., Fomel, S., and Claerbout, J. F. (1998). Regularizing velocity estimation using geologic dip information. *SEG, Expanded Abstracts*.
- [Coléou et al., 2019] Coléou, T., Formento, J.-L., Prigent, H., Messud, J., Laurencin, D., Reinier, M., Guillaume, P., Egretéau, A., and Damian, L. (2019). Use of tomography velocity uncertainty in grv calculation. *81st EAGE Conference and Exhibition, Workshop*.
- [Cowan, 1998] Cowan, G. (1998). *Statistical Data Analysis*. Oxford Science Publications.
- [Duffet and Sinoquet, 2002] Duffet, C. and Sinoquet, D. (2002). Quantifying geological uncertainties in velocity model building. *72nd SEG Annual Meeting, Expanded Abstracts*, pages 926–929.
- [Duffet and Sinoquet, 2006] Duffet, C. and Sinoquet, D. (2006). Quantifying uncertainties on the solution model of seismic tomography. *Inverse Problems*, 22(5):525–538.
- [Fournier et al., 2013] Fournier, A., Ivanova, N., Yang, Y., Osypov, K., Yarman, C., Nichols, D., Bachrach, R., You, Y., Woodward, M., and Centanni, S. (2013). Quantifying e&p value of geophysical information using seismic uncertainty analysis. *75th EAGE Conference and Exhibition*.
- [Guillaume et al., 2008] Guillaume, P., Lambaré, G., Leblanc, O., Mitouard, P., Le Moigne, J., Montel, J., Prescott, A., Siliqi, R., Vidal, N., Zhang, X., and Zimine, S. (2008). Kinematic invariants: an efficient and flexible approach for velocity model building. *78th SEG Annual Meeting, Expanded Abstracts*, pages 3687–3692.
- [Guillaume et al., 2011] Guillaume, P., Lambaré, G., Sioni, S., Carotti, D., Dépré, P., Cullianez, G., Montel, J.-P., Mitouard, P., Depagne, S., Frehers, S., and Vosberg, H. (2011). Geologically consistent velocities obtained by high definition tomography. *81st SEG Annual Meeting, Expanded Abstracts*, pages 4061–4065.
- [Guillaume et al., 2013a] Guillaume, P., Reinier, M., Lambaré, G., Cavalié, A., Adamsen, M., and Bruun, B. (2013a). Dip constrained non-linear slope tomography - an application to shallow channel characterization. *75th EAGE Conference and Exhibition*, (Tu 02 09).
- [Guillaume et al., 2013b] Guillaume, P., Zhang, X., Prescott, A., Lambaré, G., Reinier, M., Montel, J.-P., and Cavalié, A. (2013b). Multi-layer non-linear slope tomography. *75th EAGE Conference and Exhibition*, (Th 04 01).
- [Hajnal and Sereda, 1981] Hajnal, Z. and Sereda, I. T. (1981). Maximum uncertainty of interval velocity estimates. *Geophysics*, 46(11):1543–1547.
- [Lambaré, 2008] Lambaré, G. (2008). Stereotomography. *Geophysics*, 73(5):VE25–VE34.
- [Lambaré et al., 2014] Lambaré, G., Guillaume, P., and Montel, J.-P. (2014). Recent advances in ray-based tomography. *76th EAGE Conference and Exhibition*, (We G103 01).
- [Li et al., 2014] Li, L., Caers, J., and Sava, P. (2014). Uncertainty maps for seismic images through geostatistical model randomization. *SEG, Expanded Abstracts*, pages 1496–1500.
- [Messud et al., 2017a] Messud, J., Guillaume, P., and Lambaré, G. (2017a). Estimating structural uncertainties in seismic images using equi-probable tomographic model. *79th EAGE Conference and Exhibition*, (Th B4 09).

- [Messud et al., 2018] Messud, J., Guillaume, P., Reinier, M., and Hidalgo, C. (2018). Migration confidence analysis: Resolved space uncertainties. *80th EAGE Conference and Exhibition*, (Th A12 09).
- [Messud et al., 2017b] Messud, J., Reinier, M., Prigent, H., Guillaume, P., Coléou, T., and Masclet, S. (February 2017b). Extracting seismic uncertainties from tomographic velocity inversion and their use in reservoir risk analysis. *The Leading Edge, SEG*, 36(2):127–132.
- [Munõz and Rath, 2006] Munõz, G. and Rath, V. (2006). Beyond smooth inversion: the use of nullspace projection for the exploration of non-uniqueness in mt. *Geophys. J. Int.*, 164(2):301–311.
- [Operto et al., 2003] Operto, S., Lambaré, G., Podvin, P., and Thierry, P. (2003). 3d ray+born migration/inversion-part2: Application to the seg/eage overthrust experiment. *Geophysics*, 68(4):1357–1370.
- [Osypov et al., 2008a] Osypov, K., Nichols, D., Woodward, M., and Yarman, C. E. (2008a). Tomographic velocity model building using iterative eigendecomposition. *70th EAGE Conference and Exhibition*, (P164).
- [Osypov et al., 2008b] Osypov, K., Nichols, D., Woodward, M., Zdraveva, O., and Yarman, C. E. (2008b). Uncertainty and resolution analysis for anisotropic tomography using iterative eigendecomposition. *SEG, Expanded Abstracts*, pages 3244–3249.
- [Osypov et al., 2010] Osypov, K., Nichols, D., Yang, Y., Qiao, F., O’Brian, M., and Zdraveva, O. (2010). Quantifying structural uncertainty in anisotropic depth-imaging. gulf of mexico case study. *72nd EAGE Conference and Exhibition*, (CO 31).
- [Osypov et al., 2011] Osypov, K., O’Brian, M., Whitfield, P., Nichols, D., Douillard, A., Sexton, P., and Jouselin, P. (2011). Quantifying structural uncertainty in anisotropic model building and depth imaging: Hild case study. *73rd EAGE Conference and Exhibition*, (FO 10).
- [Osypov et al., 2013] Osypov, K., Yang, Y., Fourier, A., Ivanova, N., Bachrach, R., Yarman, C. E., You, Y., Nichols, D., and Woodward, M. (2013). Model-uncertainty quantification in seismic tomography: method and applications. *Geophysical Prospecting*, 61(6):1114–1134.
- [Paige and Saunders, 1982] Paige, C. C. and Saunders, M. A. (1982). Lsq: An algorithm for sparse linear equations and sparse least squares. *ACM Transactions on Mathematical Software*, 8(2):43–71.
- [Reinier et al., 2017] Reinier, M., Messud, J., Guillaume, P., and Rebert, T. (2017). Tomographic model uncertainties and their effect on imaged structures. *79th EAGE Conference and Exhibition, Workshop*.
- [Simpson et al., 2000] Simpson, G., Lamb, F., Finch, J., and Dinnie, N. (2000). The application of probabilistic and qualitative methods to asset management and decision making. *SPE*, (59455-MS).
- [Tarantola, 1986] Tarantola, A. (1986). A strategy for nonlinear elastic inversion of seismic reflection data. *Geophysics*, 51(10):1893–1903.
- [Tarantola, 2005] Tarantola, A. (2005). *Inverse Problem Theory and Methods for Model Parameters Estimation*. Society for Industrial and Applied Mathematics (Philadelphia).

- [Thore et al., 2002] Thore, P., Shtuka, A., Lecour, M., Ait-Ettajer, T., and Cognot, R. (2002). Structural uncertainties: Determination, management, and applications. *Geophysics*, 67(3):840852.
- [Virieux and Operto, 2009] Virieux, J. and Operto, S. (2009). An overview of full-waveform inversion in exploration geophysics. *Geophysics*, 74(6):WCC1WCC26.
- [Woodward et al., 2008] Woodward, M., Nichols, D., Zdraveva, O., Whitfield, P., and Johns, T. (2008). A decade of tomography. *Geophysics*, 73(5):VE5VE11.
- [Zhang and Thurber, 2007] Zhang, H. and Thurber, C. H. (2007). Estimating the model resolution matrix for large seismic tomography problems based on lanczos bidiagonalization with partial reorthogonalization. *Geophys. J. Int.*, 170(1):337–345.
- [Zhang and McMechan, 1995] Zhang, J. and McMechan, G. A. (1995). Estimation of resolution and covariance for large matrix inversions. *Geophys. J. Int.*, 121(2):409–426.